

Large family of two-dimensional ferroelectric metals discovered via machine learning

Xing-Yu Ma¹, Hou-Yi Lyu^{1,2}, Kuan-Rong Hao¹, Yi-Ming Zhao², Xiaofeng Qian³, Qing-Bo Yan^{2*}, Gang Su^{4,1*}

¹School of Physical Sciences, University of Chinese Academy of Sciences, Beijing 100049, China.

²Center of Materials Science and Optoelectronics Engineering, College of Materials Science and Optoelectronic Technology, University of Chinese Academy of Sciences, Beijing 100049, China.

³Department of Materials Science and Engineering, College of Engineering and College of Science, Texas A&M University, College Station, Texas 77843, USA.

⁴Kavli Institute for Theoretical Sciences, and CAS Center for Excellence in Topological Quantum Computation, University of Chinese Academy of Sciences, Beijing 100190, China.

*Correspondence authors.

E-mail addresses: yan@ucas.ac.cn (Q. B. Yan), gsu@ucas.ac.cn (G. Su).

ABSTRACT

Ferroelectricity and metallicity are usually believed not to coexist because conducting electrons would screen out static internal electric fields. In 1965, Anderson and Blount proposed the concept of “ferroelectric metal”, however, it is only until recently that very rare ferroelectric metals were reported. Here, by combining high-throughput *ab initio* calculations and data-driven machine learning method with new electronic orbital based descriptors, we systematically investigated a large family (2,964) of two-dimensional (2D) bimetal phosphates, and discovered 60 stable ferroelectrics with out-of-plane polarization, including 16 ferroelectric metals and 44 ferroelectric semiconductors that contain seven multiferroics. The ferroelectricity origins from spontaneous symmetry breaking induced by the opposite displacements of bimetal atoms, and the full-*d*-orbital coinage metal elements cause larger displacements and polarization than other elements. For 2D ferroelectric metals, the odd electrons per unit cell without spin polarization may lead to a half-filled energy band around Fermi level and is responsible for the metallicity. It is revealed that the conducting electrons mainly move on a single-side surface of the 2D layer, while both the ionic and electric contributions to polarization come from the other side and are vertical to the above layer, thereby causing the coexistence of metallicity and ferroelectricity. Van der Waals heterostructures based on ferroelectric metals may enable the change of Schottky barrier height or the Schottky-Ohmic contact type and induce a dramatic change of their vertical transport properties. Our work greatly expands the family of 2D ferroelectric metals and will spur further exploration of 2D ferroelectric metals.

Keywords:

ferroelectric metal; 2D ferroelectricity; multiferroics; *ab initio* calculations; Machine learning

1. Introduction

Since the successful exfoliation of graphene [1] in 2004, numerous two-dimensional (2D) materials with extraordinary properties and rich potential applications have been discovered [2-4]. Ferroelectricity is an intriguing character of materials with switchable spontaneous electric polarization, which was generally believed to decay and even disappear if the film thickness is below a critical value [5-8]. For instance, BaTiO₃ thin films lose their ferroelectricity below a critical thickness of about six unit cells [9]. However, several 2D materials have recently been reported to be ferroelectrics, including Group IV monochalcogenides [10-12], 1T monolayer MoS₂ [13], buckled CrN and CrB₂ [14], In₂Se₃ and other III₂-VI₃ compounds [15,16], MXenes (Sc₂CO₂) [17], AgBiP₂Se₆, CuMP₂X₆ (M=Cr, V; X=S, Se) and CuInP₂S₆ [18-21], in contrast to the conventional notion that ferroelectricity would disappear in 2D limit [5-8], suggesting an underexplored exciting realm of 2D materials.

It is often thought that ferroelectricity and metallicity cannot coexist in a metal because conduction electrons would screen out static internal electric field that arises from dipole moment, thereby precluding intrinsic ferroelectric polarization [22,23]. In 1965, Anderson and Blount introduced the concept of ‘ferroelectric metal’ and proposed that the polar structure possibly appears in certain martensitic transitions involving the inversion symmetry breaking [24]. Recently, polar metals (e.g., LiOsO₃ and chemically tuned MoTe₂) have been reported [25,26]. Monolayer CrN and layered Bi₅Ti₅O₁₇ are also predicted to be ferroelectric metals [14,27]. More interestingly, two- or three-layer WTe₂ have been found to exhibit spontaneous electric polarization that can be switched using an external electric field [23], which may be the first experimental evidence for the coexistence of ferroelectricity and metallicity in a 2D material. Very recently, ferroelectricity driven nonlinear anomalous Hall current switching was proposed and the time-reversal invariance was experimentally demonstrated in odd-layer WTe₂ [28-30]. Nevertheless, until now, the examples of ferroelectric metals are still extremely sparse.

By combining high-throughput *ab initio* calculations and a data-driven machine learning model with new electronic orbital-based descriptors, here we systematically investigated a large family (2,964) of 2D bimetal phosphates, and discovered total 60 stable ferroelectrics, including 16 ferroelectric metals and 44 ferroelectric semiconductors

among which seven multiferroics and seven ferroelectric water-splitting photocatalysts are screened out. The physical origin of ferroelectricity in these 16 2D ferroelectric metals is owing to the spontaneous symmetry breaking induced by the opposite vertical displacements of bimetal atoms. The ferroelectric-paraelectric transitions were simulated, revealing that the polarization could be reversed by a vertical external electric field. These ferroelectric metals possess odd electrons in a unit cell, in which conducting electrons mainly distribute on a single-side surface, while the ionic and electric contributions to polarization come from the other side, causing the coexistence of ferroelectricity and metallicity. The present work highly enriches the family of ferroelectric metals, suggesting that ferroelectric metals could be achievable in 2D materials. As ferroelectric metals could be constructed van der Waals heterostructures that may have wide applications in areas of ferroelectric tunneling junction, nonvolatile ferroelectric memory, etc., our proposal would spur great interest in exploring 2D ferroelectric metals in physics, materials sciences and information technology.

2. Materials and methods

The density functional theory first-principles calculations are performed by projected augmented wave (PAW) [31] implemented Vienna *ab initio* simulation package (VASP) [32]. The exchange-correlation interactions are treated using Perdew-Burke-Ernzerhof generalized gradient approximation (PBE-GGA) [33]. Cut-off energy of 450 eV was set for the plane-wave basis and $10 \times 10 \times 1$ k-points are used to sample the Brillouin zone. The convergence criteria were 1×10^{-6} eV for the energy difference in the electronic self-consistent calculation and 1×10^{-3} eV/Å for the residual forces on lattice geometries and atomic positions. All electronic structures are calculated using the PBE+ U method. For the on-site Coulomb interaction U of the 3d, 4d and 5d transition metals, $U = 4, 2.5,$ and 0.5 eV are used, respectively, which are usually reasonable for them [34,35]. The all magnetic configurations are considered on $2 \times 2 \times 1$ unit cell. See the Supplementary materials for more details.

3. Results and Discussion

3.1 Structures of 2D bimetal phosphates

Fig. 1a illustrates the schematic structure of 2D bimetal phosphates ($M_I M_{II} P_2 X_6$, M_I and M_{II} atoms are different metal elements, X is chalcogen atom), which contains a honeycomb lattice (indicated by dash lines) formed by staggering metal atoms M_I (blue balls) and M_{II} (red balls), and P-P pairs (yellow balls) are located vertically at the center of hexagons. Chalcogen atoms (green balls) bridge metal atoms and P-P pairs, and each metal or phosphorous atom is surrounded by six or three chalcogen atoms, respectively. As indicated in Fig. 1b, if M_I and M_{II} atoms locating on the plane bisect perpendicularly the P-P pairs, the whole structure has a space group $P-6m2$ (No.187) (or $P312$ (No. 149), $P222$ (No.16) for some materials), which corresponds to non-polar point groups $-6m2$ (or $32, 222$) and is denoted as “high-symmetry phase”. Interestingly, among all 2D $M_I M_{II} P_2 X_6$ materials, we found two types of possible spontaneous geometric symmetry reduction: (i) Type-I in Fig. 1c, M_I and M_{II} atoms deviate from the bisect plane (indicated with grey color) in opposite directions with displacements d_1 and d_2 , respectively, and the total relative vertical displacement between M_I and M_{II} atoms is $d=d_1+d_2$. Meanwhile, the space groups reduce to $P3m1$ (No. 156) (or $P3$ (No. 143), $P1$ (No. 1)), which corresponds to polar point group $3m$ (or $3, 1$). (ii) Type-II in Fig. 1d, where the whole structure is distorted with P-P pairs inclining to three different directions, forming three symmetry-equivalent phases (α, β , and γ) with space groups Cm (No. 8) (or $P1$), which corresponds to polar point group m (or 1). Our calculations reveal that the high-symmetry phase, Type-I and Type-II low-symmetry phases are paraelectric, ferroelectric, and ferroelastic (with ferroelectric), respectively.

Based on the above 2D bimetal phosphate prototype, we generate different structures of $M_I M_{II} P_2 X_6$ by replacing M_I and M_{II} with 39 metal elements (Table S1 online) and replacing X by four chalcogen atoms (O, S, Se, and Te), respectively. The total number of such structures is 2,964, in which stoichiometrically equivalent structures are excluded, i.e., $M_I M_{II} P_2 X_6$ and $M_{II} M_I P_2 X_6$ are treated as the same material. A thorough first-principles investigation on such a large amount of materials would be extremely time-consuming. Here we use data-driven machine learning method by introducing new descriptors and combine with high-throughput *ab initio* calculations to accelerate the discovery of ferroelectrics from 2,964 structures of $M_I M_{II} P_2 X_6$ materials.

3.2 Machine learning model

The workflow is schematically illustrated in Fig. 2. Among 2,964 $M_{\text{I}}M_{\text{II}}P_2X_6$ structures, 605 of them are randomly selected as the initial training/test dataset for training a machine learning classification model. The structural optimization and corresponding properties were calculated by first-principles density functional theory (DFT) (the calculation details can be found in Materials and methods). Based on the results of these DFT calculations, 103 ferroelectrics (FE) were identified with a simplified criterion (Fig. S1 online). In the training of machine learning model, the materials in the dataset are described by 35 initial features (descriptors) (Table S2 online), including novel orbital-based descriptors designed by us, which were proved essential for a high-precision prediction (Table S3 online). Feature reduction was performed, and top 10 features were obtained to construct optimal feature space (Fig. S3 online). Five different machine learning algorithms such as the support vector classifier (SVC) [36], random forest classifier (RFC) [37], adaboost classifier [38], decision trees classifier (DTC) [39] and gradient boosting classifier (GBC) [40] were tested, all of which have been successfully applied to predict various materials [41,42]. The results of 5-fold cross-validation analysis and grid search for optimal hyper-parameters show that the GBC model outperforms the other four and gives the best performance (Fig. S2 online). Consequently, GBC was adopted in our model.

The precision of the initially obtained results was only 64%. To improve the performance, we introduced the data-driven methodology recently applied in materials and chemical sciences [43,44]. With the initial classification model, we obtained the prediction probability (Prob) of the remaining unexplored $M_{\text{I}}M_{\text{II}}P_2X_6$ structures and then labeled them as a positive or negative class with the criteria $\text{Prob} \geq 0.5$ or $\text{Prob} < 0.5$, respectively. Those with the prediction probability near the dividing line, i.e., $0.45 \leq \text{Prob} \leq 0.55$, were added to the training/test dataset. Based on the updated dataset, a new machine learning model could be obtained with improved precision. The above process was repeated until the model precision converges, which occurs at the fourth iteration (Figs. S5a online). Subsequently, a total of 293 extra $M_{\text{I}}M_{\text{II}}P_2X_6$ materials were added to the training/test dataset. In the end, we obtained an optimal machine learning model with high precision (77.2%) and high AUC (the area under the receiver operating

characteristic curve) value (88.3%) (Fig. S5a and b online), showing that the data-driven methodology improved remarkably the performance of the machine-learning model. With this optimal classification model, 166 potential ferroelectrics are screened out from the remaining unexplored 2066 bimetal phosphates. Together with those 279 ferroelectrics identified in the updated training/test dataset, we obtained 445 potential ferroelectrics bimetal phosphates.

3.3 Ferroelectrics

As shown in the right panel of Fig. 2, we then performed systematic DFT calculations for these 445 ferroelectric candidates to acquire the optimized geometric structures with magnetic ground states. Their dynamical stabilities were examined by using density functional perturbation theory (DFPT) calculations [45], which yields 60 dynamically stable ferroelectric bimetal phosphates out of 445 candidates. In addition, their thermodynamic stabilities have been verified with the heat of formation (see details in the Supplementary materials). It should be mentioned that the energy above the convex hull can also be adopted to check the thermodynamic stability of a structure, which needs the information of its bulk phase [46]. As the present 2D structures have no corresponding bulk phases in databases, we opt to use the heat of formation to inspect their thermodynamic stabilities. They are displacive-type ferroelectrics, as their physical origin of ferroelectricity is owing to the spontaneous symmetry breaking mainly induced by vertical displacements of M_I and M_{II} atoms as shown in Fig. 1. For these 60 ferroelectric $M_I M_{II} P_2 X_6$ materials, we observed a quadratic relation between the out-of-plane polarization (P) and the relative vertical displacement (d) between metal atoms M_I and M_{II} (Fig. S6 online), i.e., $P \propto d^2$, providing a practical approach for rapidly identifying ferroelectric bimetal phosphates candidates with large electric polarization. It is quite different from the case of ferroelectric inorganic perovskites, in which the polarization is linearly correlated with the displacement [47].

The systematic DFT calculations on electronic structures of these 60 2D ferroelectric materials reveal that 16 of them are ferroelectric metals and the other 44 are ferroelectric semiconductors. This large family of novel ferroelectric metals will be discussed in detail below. Surprisingly, seven out of 44 stable ferroelectric semiconductors $M_I M_{II} P_2 X_6$

exhibit the coexistence of two or three types of ferroic orderings such as ferromagnetic, antiferromagnetic, ferroelectric, and ferroelastic orderings, i.e., 2D multiferroics. Specifically, InHgP_2O_6 is a multiferroic material with the coexistence of ferroelectricity and ferromagnetism (FE+FM), NbCuP_2S_6 and PtMoP_2O_6 can accommodate both ferroelectricity and antiferromagnetism (FE+AFM), GaAuP_2O_6 is multiferroic with ferroelectricity and ferroelasticity (FE+FEA), while AlZrP_2O_6 , HgIrP_2O_6 , and PtOsP_2O_6 possess simultaneously three ferroic orderings including ferroelectricity, ferroelasticity, and antiferromagnetism, giving rise to FE+FEA+AFM multiferroics. These multiferroic materials may have potential applications in magnetoelectric, magnetostrictive, or mechanic-electric nanodevices. Besides, it is also interesting to examine their possibilities as photocatalytic materials for water-splitting, as it was reported that ferroelectricity may be beneficial to improve the photocatalytic performance because the built-in electric field hinders the recombination of photogenerated electrons and holes [48,49]. Seven ferroelectric semiconductors, including ZrZnP_2O_6 , CdHfP_2O_6 , GaLaP_2S_6 , $\text{CuTiP}_2\text{Se}_6$, CuYP_2S_6 , CuScP_2S_6 , and AuScP_2S_6 , were indeed found to have suitable band edges and band gaps (1.59–2.50 eV) for water-splitting photocatalysts (Table S8 online).

3.4 Ferroelectric metals

Table 1 lists the formula and properties of 16 ferroelectric metals $\text{M}_\text{I}\text{M}_\text{II}\text{P}_2\text{X}_6$, and Fig. S11 (online) presents their geometric structures. They are non-centrosymmetric with space group of $P3$ or $P3m1$, corresponding to the “low-symmetry phase” in Fig. 1c, and the corresponding electric polarizations point to the z -direction (out-of-plane). As aforementioned, we denoted the absolute values of displacements of M_I and M_II atoms with d_1 and d_2 , where the displacements move toward opposite directions for all above ferroelectric metals, leading to the relative vertical displacement between M_I and M_II atoms is $d = d_1 + d_2$, as indicated in Fig. 1c. Considering that $\text{M}_\text{I}\text{M}_\text{II}\text{P}_2\text{X}_6$ and $\text{M}_\text{II}\text{M}_\text{I}\text{P}_2\text{X}_6$ represent the same material, the order of M_I and M_II in the formulas in Table 1 is arranged to assure $d_1 > d_2$, which means that M_I contributes primarily to the displacement and polarization for each $\text{M}_\text{I}\text{M}_\text{II}\text{P}_2\text{X}_6$. These 16 ferroelectric metals in Table 1 are sorted by polarization (pC/m) in ascending order. We have several interesting observations in order. (i) The ferroelectric metals with high polarization all contain coinage metal

elements (Au, Ag, or Cu); (ii) the increasing trend of polarization with d_1 has similarity more than with d_2 (Fig. S7 online), implying that the displacements of M_I atoms dominate the polarization; (iii) besides Au, Ag, and Cu, M_I elements are In, Ga, Sn or Pb of IIIA or IVA metal elements. By carefully checking the values of d_1 (d_2) of each element, we can divide the metal elements in ferroelectric metal $M_I M_{II} P_2 X_6$ into three groups: Group A includes coinage metal elements (Au, Ag, or Cu) with large displacements ($> 0.62 \text{ \AA}$); Group B includes IIIA and IVA metal elements (In, Ga, Sn, and Pb) with moderate displacements (between 0.32 and 0.61 \AA); and Group C includes other transition metal elements (Y, Zr, Hf) with small displacements ($< 0.28 \text{ \AA}$). The coinage metal elements and IIIA/IVA metal elements lead to displacements larger than other transition metal elements. We can understand this behavior as follows. In the high-symmetry (paraelectric) phase of $M_I M_{II} P_2 X_6$, the metal atoms locate in the bisector of P-P pair ($d_1 = d_2 = d = 0$), implying that metal atoms should be bonded with both upper-three and lower-three chalcogen X atoms (Fig. 1a and b), i.e., metal atoms are octahedrally coordinated with six chalcogen atoms, just like that in 1T-MoS₂ and other transition metal dichalcogenides (TMDCs) [50]. However, coinage metal elements and IIIA/IVA metal elements have full d -orbitals and do not tend to form the octahedrally coordinated bonding. In contrast, they tend to bond only with either upper-three or lower-three chalcogen X atoms, which manifests that the metal atoms will deviate from their original high-symmetric positions, resulting in the spontaneous symmetry breaking and the emergence of the out-of-plane polar axis. Thus, the coinage metal elements and IIIA/IVA metal elements (Group B) with full d -orbital, in particular Au, Ag, and Cu, can lead to large displacement and high polarization. It also explains why electronic orbital-based descriptors are essential for high-precision prediction in our machine learning model (Fig. S5c online).

Since the metal atoms in above three groups can have distinct displacements, various combinations of M_I and M_{II} metals may lead to diverse physical properties. Here we focus on AuZrP₂S₆ and InZrP₂Te₆ as typical examples of Group A+C and Group B+C combinations, respectively. As d_1 of AuZrP₂S₆ (1.63 \AA) is about three times of InZrP₂Te₆ (0.52 \AA), the polarization of AuZrP₂S₆ (9.740 pC/m) is about five times of InZrP₂Te₆ (1.822 pC/m). Fig. 3a and b show the energy bands of InZrP₂Te₆ and AuZrP₂S₆, respectively. The energy bands are almost unaltered when the spin-orbit coupling (SOC)

is considered (Figs. S14 and S17 online). For each of $\text{InZrP}_2\text{Te}_6$ and AuZrP_2S_6 , there is a single energy band crossing the Fermi level, indicating a metallic character. This energy band separated from other bands by distinct gaps is exactly half-filling, showing that the number of total valence electrons per unit cell should be odd, as indeed shown in Table 1 for $\text{InZrP}_2\text{Te}_6$ and AuZrP_2S_6 . Other ferroelectric metals exhibit similar characters in energy bands (Figs. S14–S17 online) and electron parity, implying that they share similar electronic properties and the same metallic mechanism. Thus, in all 16 ferroelectric metals we find that a unit cell contains an odd number of electrons, which may lead to a half-filled energy band across the Fermi level, and gives rise to the metallicity. The odd valence electrons in a unit cell appear to be a necessary (but not a sufficient) condition for a ferroelectric metal in $\text{M}_I\text{M}_{II}\text{P}_2\text{X}_6$ materials. There are exceptions when the system is spin-polarized however. For instance, InHgP_2O_6 (Fig. S19a online) has odd valence electrons and its energy band around Fermi level splits into a fulfilled spin-up band and an empty spin-down band with a gap, thus, it is a non-metallic multiferroic with ferroelectric and ferromagnetic orderings. For non-magnetic ferroelectric semiconductors, the number of total valence electrons in a unit cell is even (Table S8 and S9 online), because the even number of electrons in a unit cell would have no unpaired electrons for this family of materials, usually leading to semiconductors.

The projected electronic density of states (PDOS) of AuZrP_2S_6 and $\text{InZrP}_2\text{Te}_6$ are presented in Fig. 3c and d. For $\text{InZrP}_2\text{Te}_6$, the electronic states at the Fermi level are mainly contributed by the p electrons of Te atoms. Similar electronic structures are also observed in other Group B+C materials (such as PbYP_2Te_6 and $\text{InHfP}_2\text{Te}_6$, see Figs. S16 and S17 online). In contrast, the electronic states at the Fermi level in AuZrP_2S_6 are mainly contributed by d electrons of Zr atoms and p electrons of S atoms. Similar electronic structures are also observed in other Group A+C materials (such as AgZrP_2S_6 , $\text{CuHfP}_2\text{Se}_6$, and CuZrP_2S_6 , see Figs. S14 and S15 online). $\text{AuSnP}_2\text{Te}_6$ is a typical Group A+B material, hence there is also a single energy band crossing the Fermi level, but it is mainly contributed by p electrons of Te atoms and s electrons of Sn atoms (Fig. S16 online). Therefore, in Group B+C materials, the p electrons of chalcogen atoms have a dominant contribution to the conducting states; in Group A+C materials, both transition-metal d -orbitals and chalcogen p -orbitals dominate the conducting states; while

in Group A+B materials, the chalcogen p -orbitals and s -orbitals of IIIA/IVA metal atoms contribute mainly to the conducting states. In all types of above ferroelectric metals, the chalcogen p -orbitals play a crucial role in the conduction.

Now we visualize the partial electron densities of $\text{InZrP}_2\text{Te}_6$ and AuZrP_2S_6 within energy range $|E-E_f| < 0.05$ eV, which are usually considered as the conducting electron density $\rho_c(\vec{r})$ (Details can be found in the Supplementary materials). As shown in Fig. 3e, $\rho_c(\vec{r})$ of $\text{InZrP}_2\text{Te}_6$ exhibits a p -orbital character around Te atoms; in contrast, $\rho_c(\vec{r})$ of AuZrP_2S_6 shows a p - d hybridization character around Zr and S atoms as indicated in Fig. 3f, both being consistent with the observations from PDOS. The conducting electrons of $\text{InZrP}_2\text{Te}_6$ and AuZrP_2S_6 constitute a C3-symmetry connecting network with a few low-density hollows, which may provide conducting channels in real space. The left panels of Fig. 3g and h show the side views of an isosurface of $\rho_c(\vec{r})$. It is surprising to observe that $\rho_c(\vec{r})$ of $\text{InZrP}_2\text{Te}_6$ and AuZrP_2S_6 are mainly distributed on the upper surface of the 2D layer and are weakly relevant to In and Au atoms (indicated with blue color) of the lower surface. Note that In and Au are M_I atoms, which have large displacements and are major contributors for the electric polarization. We define a ‘reduced’ conducting electron density by integrating $\rho_c(\vec{r})$ over the x - y plane, say, $\rho_c(z) = \iint \rho_c(\vec{r}) dx dy$, where $\rho_c(\vec{r})$ is the conducting electron density. The results are shown in the right panels of Fig. 3g and h, which indicate clearly that the conducting electrons mainly move on the upper surface. When M_I atoms move to the lower surface, the coordinate number for chalcogen atoms on the upper surface could be reduced and excessive electrons emerge, which may partially fill the energy band around Fermi level and contribute to the conduction.

To describe the spatial distribution of electrons that contribute to the electric polarization, we introduce a “reduced” difference charge density defined as $\rho_p(z) = \iint [\rho_{\text{FE}}(\vec{r}) - \rho_{\text{PE}}(\vec{r})] dx dy$, where $\rho_{\text{FE}}(\vec{r})$ and $\rho_{\text{PE}}(\vec{r})$ are the total electron densities of a ferroelectric material in ferroelectric and paraelectric phases, respectively. Since the paraelectric phase has a high symmetric structure and zero polarization, $\rho_{\text{PE}}(\vec{r})$ has no contribution to polarization. The difference between $\rho_{\text{FE}}(\vec{r})$ and $\rho_{\text{PE}}(\vec{r})$ can reflect the electronic contribution to the polarization, and we term $\rho_p(z)$ as the reduced “FE-PE electron density difference”. As shown in the right panels of Fig. 3g and h, $\rho_p(z)$

exhibits an oscillating behavior and reveals the spatial distribution of charge polarization. $\rho_p(z)$ of AuZrP_2S_6 is closer to the lower surface than that of $\text{InZrP}_2\text{Te}_6$, which is consistent with the fact that the displacement of Au atoms is larger than that of In atoms, and Au atoms are also closer to the lower surface of the 2D layer. For both materials $\rho_c(z)$ deviates obviously from that of $\rho_p(z)$, i.e., the conducting electrons and “FE-PE electrons density difference” are spatially separated, providing clues on the underlying mechanism of ferroelectric metallicity in these 2D $\text{M}_I\text{M}_{II}\text{P}_2\text{X}_6$ metals.

The coexistence of ferroelectricity and metallicity in 2D $\text{M}_I\text{M}_{II}\text{P}_2\text{X}_6$ materials can be rationalized as follows. First, the chemical nature of coinage metal elements and IIIA/IVA metal elements (M_I site) make them deviate from high-symmetric positions and move to the lower surface (Fig. 3g and h), which have large displacements and make the major ionic contribution to electric polarization. In contrast, the displacements of M_{II} atoms are tiny, resulting in a rather weak effect. Along with atomic displacements, the “FE-PE electron density difference” distributes mainly in the lower part of the 2D layer. Thus, the total polarization including ionic and electronic contributions is related to the lower part of 2D $\text{M}_I\text{M}_{II}\text{P}_2\text{X}_6$ materials. Second, when the total number of valence electrons in a unit cell is odd, and the system is not spin-polarized, the energy band around Fermi level should be half-filled, leading to a metallic property. M_I atoms move to the lower surface and leave unsaturated chalcogen atoms and excessive electrons on the upper surface, which contribute to the conduction. Third, the conducting electron density dominantly distributes around the chalcogen atoms and M_{II} atoms in the upper surface, which cannot completely screen the vertical polarization that mainly comes from the lower part of the 2D layer. In addition, the low-density hollows are observed in conducting electron density (Fig. 3e and f), which implies that the conducting electrons may not completely exclude the external electric fields. Our analyses reveal that the coexistence of ferroelectricity and metallicity here is the consequence of a dimensionality effect. These findings suggest that ferroelectric metals could be highly achievable in 2D materials.

3.5 Ferroelectric-paraelectric phase transition and polarization reversal

The phase transition between ferroelectric and paraelectric phases is an essential character of ferroelectric materials and crucial for possible applications. We simulated the polarization reversal paths of these 16 ferroelectric metals $M_I M_{II} P_2 X_6$ by using the climbing image nudged elastic band (CI-NEB) method [51]. The ferroelectric-paraelectric transition barriers are obtained, as listed in Table 1, which range from 0.04 to 0.57 eV/unit cell. The barriers generally increase with the increase of displacement of M_{II} atoms (d_2) (see Fig. S8b online). For two ferroelectric metals, $AuHfP_2O_6$, and $AuZrP_2O_6$, as shown in Fig. 4a and b, the energy versus polarization profiles exhibit common double-well shape and clear bistability, where two minima correspond to ferroelectric phases of opposite polarizations, while the maximum corresponds to paraelectric phase (see Fig. 4a, b for energy versus polarization profiles of $AuHfP_2O_6$, and $AuZrP_2O_6$). The Landau-Ginzburg theory was applied to deal with ferroelectric phase transitions. We take polarization \mathbf{P} as the order parameter of ferroelectric phase. The Landau-Ginzburg expansion has the form of $E = \sum_i \left[\frac{A}{2} P_i^2 + \frac{B}{4} P_i^4 + \frac{C}{6} P_i^6 \right] + \frac{D}{2} \sum_{\langle i,j \rangle} (P_i - P_j)^2$. Here P_i is the polarization of i -th unit cell, $\langle i,j \rangle$ indicates the nearest neighbors, and A , B , C , D are coefficients. The energy versus polarization profiles in Fig. 4 is fitted using the first three terms. The last term describes the dipole-dipole interaction between nearest neighboring unit cells. All the coefficients are obtained by fitting to DFT results, as listed in Table S11 (online). Based on this model, ferroelectric Curie temperatures T_c are obtained using Monte Carlo (MC) simulation, which was frequently employed to estimate ferroelectric transition temperature T_c in previous works [52,53]. It is predicted that T_c of $AuZrP_2O_6$ and $AuHfP_2O_6$ is 2050 and 800 K (Fig. S25 online), respectively, which are much higher than room temperature, showing that the ferroelectricity of these metals is very robust under thermal perturbations. The ultrahigh T_c of $AuZrP_2O_6$ may be due to strong dipole-dipole interaction (D) between nearest neighboring unit cells.

As aforementioned, bilayer WTe_2 is the first experimental evidence for the coexistence of ferroelectricity and metallicity in 2D materials, which has a polarization of 0.375 pC/m (2.00×10^{11} e/cm²) at 20 K [23]. Our calculated polarization for bilayer WTe_2 is 0.423 pC/m (2.35×10^{11} e/cm²), in good agreement with the experimental value, indicating our

calculations are reliable. As listed in Table 1, we find that the polarization of 16 ferroelectric metals $M_I M_{II} P_2 X_6$ is about one order of magnitude higher than bilayer WTe_2 . Besides, the Curie temperatures are also considerably higher than that of bilayer WTe_2 . Thus, the robustness of metallic ferroelectricity in $M_I M_{II} P_2 X_6$ is stronger than that in bilayer WTe_2 , implying that the coexistence of ferroelectricity and metallicity in $M_I M_{II} P_2 X_6$ may be easily experimentally detected than in bilayer WTe_2 .

Generally, the polarization of a ferroelectric material can be switched by applying a proper electric field, which was successfully demonstrated in bilayer WTe_2 [23]. We further calculated the energy versus polarization profiles under different vertical electric fields for $AuHfP_2O_6$ and $AuZrP_2O_6$. As shown in Fig. 4c and d, one may see that with increasing the electric field, the energies increase for $P\downarrow$ polarization and decrease for $P\uparrow$ polarization, which makes the energy barrier from $P\downarrow$ to $P\uparrow$ polarization decrease dramatically. It turns out that an electric field of 1.0 V/\AA gives rise to small energy barriers of 10 and 26 meV/unit cell for $AuHfP_2O_6$ and $AuZrP_2O_6$, respectively, which suggests that 1.0 V/\AA may be the critical electric field for reversing polarization at room temperature. Note that the structures cannot be destroyed until the electric field is higher than 2.8 V/\AA . This critical electric field (1.0 V/\AA) is nearly the same order of magnitude as that of 2D ferroelectric In_2Se_3 (0.66 V/\AA) [15]. As the electric polarization of the latter can be switched by gate voltage experimentally [54], the polarization of $AuHfP_2O_6$ and $AuZrP_2O_6$ could likewise be switched by a proper external electric field.

3.6 Van der Waals heterostructures based on ferroelectric metal

The coexistence of ferroelectricity and metallicity in $M_I M_{II} P_2 X_6$ may bring various potential applications. The most intriguing property of 2D ferroelectric metal $M_I M_{II} P_2 X_6$ is the fact that conducting electrons distribute mainly on single side of 2D layer with finite thickness, which is associated with the polarization direction. If we flip the direction of polarization up or down, major conducting electrons of $M_I M_{II} P_2 X_6$ will move to the lower or upper surface of the 2D layer, which may lead to novel physical effects. The van der Waals contact between 2D ferroelectric metal and other 2D materials would be appropriate to demonstrate how the switching of polarization direction modulates the surface or interface properties of the contact. By considering lattice matching, we

constructed two types of van der Waals heterostructures as examples, i.e., AuSnP₂Te₆/graphene and AuZrP₂S₆/MoS₂. Fig. 5a and b show the energy bands of AuSnP₂Te₆/graphene heterostructure with the polarization of AuSnP₂Te₆ along *z* direction (P↑) and opposite direction (P↓), respectively. The energy bands from graphene and AuSnP₂Te₆ shift up and down relative to the Fermi level, respectively, indicating a transfer of electrons from graphene to AuSnP₂Te₆ (Fig. S27f online), while the profiles of energy bands remain intact. The shift of energy bands for graphene with polarization P↑ is larger than that for P↓, showing that the reversal of polarization of AuSnP₂Te₆ would influence the number of conducting electrons transferred (Fig. S27h online). Thus, in this heterostructure of graphene and AuSnP₂Te₆ in which both are conducting, an electric field may induce different resistive states depending on the direction of electric polarization, which may have potential applications in information storage.

Fig. 5c and d show the energy bands of AuZrP₂S₆/MoS₂ heterostructure with the polarization of AuZrP₂S₆ along *z*-direction (P↑) and opposite direction (P↓), respectively. It is interesting to note that there is still a half-filled band across Fermi level, which comes from AuZrP₂S₆ and locates in the gap of MoS₂, indicating that no charge transfers between AuZrP₂S₆ and MoS₂ layers, which is caused by the large gap of MoS₂ (~1.7 eV). Regardless of the polarization direction of AuZrP₂S₆, the Fermi level is not obviously shifted from the half-filled band, however, the energy bands from MoS₂ shift remarkably when the direction of polarization is switched from P↑ to P↓. The conduction band minima (CBM) of MoS₂ is 0.708 eV above Fermi level in AuZrP₂S₆ (P↑)/MoS₂ and 0.375 eV above Fermi level in AuZrP₂S₆ (P↓)/MoS₂ (Fig. 5c and d), which can be viewed as the Schottky barrier (Φ_e) between AuZrP₂S₆ and intrinsic MoS₂. Thus, the contact between AuZrP₂S₆ and intrinsic MoS₂ is of Schottky type, where the Schottky barrier can be modulated through the reversal of electric polarization. In addition, doping in semiconductor MoS₂ can induce an impurity level in the gap. If the impurity level (E_{im}) is below the CBM and the value of $E_{CBM} - E_{im}$ is between 0.708 and 0.375 eV, for example, fluorine doping in MoS₂ will induce an impurity level with $E_{CBM} - E_{im} = 0.5$ eV [55], the contact of AuZrP₂S₆ (P↑)/MoS₂ will still be of Schottky type, while the contact of AuZrP₂S₆ (P↓)/MoS₂ will become Ohmic type. In other words, the reversal of electric polarization can switch the contact from Schottky to Ohmic type for the heterostructure

of AuZrP₂S₆ and properly doped MoS₂. The change of the height of Schottky barrier or the Schottky-Ohmic contact type could induce a dramatic change of the transport properties along the vertical direction, and novel physical effects such as giant electroresistance [56,57] could be expected.

By combining 2D ferroelectric metals and other 2D materials, various types of van der Waals heterostructures can be generated, and their physical properties can be easily modulated through doping, an electric field or a magnetic field, etc., to make them possible potential candidates for novel devices such as ferroelectric tunneling junction with giant electroresistance, field-effect transistor, nonvolatile ferroelectric memory, etc. Besides, considering the coupling between the direction of polarization and single-side surface conducting electrons, ferroelectric metals M_IM_{II}P₂X₆ may be good materials for the use in electrical-writing/optical-reading memory and ferroelectric printing devices.

4. Conclusion

We employed high-throughput *ab initio* calculations and data-driven machine learning schemes with a set of new electronic orbital-based descriptors to discover novel 60 stable ferroelectric materials out of 2,964 structures of 2D bimetal phosphates M_IM_{II}P₂X₆, including 16 ferroelectric metals with out-of-plane electric polarization and 44 ferroelectric semiconductors. Among the 44 semiconducting ones, seven multiferroics with two or three types of ferroic orderings and seven ferroelectric water-splitting photocatalysts were screened out. For this family of 2D ferroelectric metals, the physical origin of ferroelectricity is owing to the spontaneous symmetry breaking induced by the opposite vertical displacements of two metal atoms M_I and M_{II}, where the out-of-plane polarization (\mathbf{P}) and relative vertical displacement (d) are unveiled to comply a quadratic relationship, revealing that these 16 2D ferroelectric metals belong to displacive-type ferroelectrics. The coinage metal elements with full d -orbitals, i.e., Au, Ag, and Cu, can lead to large displacements and large polarization due to the nature of their chemical bonding. We also found that odd number of valence electrons in a unit cell lead to a half-filled energy band around Fermi level and is responsible for metallicity, and chalcogen p -orbitals play an important role in the conduction in all 16 ferroelectric metals. The charge density analysis shows that the coexistence of ferroelectricity and metallicity

in $M_I M_{II} P_2 X_6$ is a consequence of dimensionality effect, in which the conducting electrons distribute mainly on the upper surface of the 2D layer, whereas the out-of-plane electric polarization induced from both ionic and electronic motion is primarily related to the lower part of the 2D layer. It shows if conducting electrons move on a 2D plane, while the electric polarization happens along the third dimension, ferroelectricity and metallicity could coexist in the same material. With this scenario, ferroelectric metals could be achievable in 2D materials. Our work presents a large family of novel 2D ferroelectric metals with intriguing properties, which could be applied to construct heterostructures through van der Waals contact that may have possible applications in areas of ferroelectric tunneling junction, nonvolatile ferroelectric memory, etc. As ferroelectric metals are still extremely sparse now, it would spur great interest in exploring 2D ferroelectric metals in near future.

Conflict of interest

The authors declare that they have no conflict of interest.

Acknowledgments

This work was supported in part by the National Key R&D Program of China (2018YFA0305800), the Strategic Priority Research Program of CAS (XDB28000000), the National Natural Science Foundation of China (11834014), Beijing Municipal Science and Technology Commission (Z191100007219013), and University of Chinese Academy of Sciences. The calculations were performed on Era at the Supercomputing Center of the Chinese Academy of Sciences and Tianhe-2 at the National Supercomputing Center in Guangzhou.

Author contributions

Qing-Bo Yan and Gang Su conceived the project and supervised the research. Xing-Yu Ma performed the calculations. Xing-Yu Ma, Qing-Bo Yan, and Gang Su developed the codes for calculating out-of-plane polarization and machine learning model, analyzed the results, and wrote the manuscript. Xiaofeng Qian participated in data analysis and

manuscript writing. Hou-Yi Lyu, Kuan-Rong Hao, and Yi-Ming Zhao participated in the discussion.

References

- [1] Novoselov KS, Geim AK, Morozov SV, et al. Electric field effect in atomically thin carbon films. *Science* 2004;306:666-669.
- [2] Mak KF, Lee C, Hone J, et al. Atomically thin MoS₂: a new direct-gap semiconductor. *Phys Rev Lett* 2010;105:136805.
- [3] Li L, Chen Z, Hu Y, et al. Single-layer single-crystalline SnSe nanosheets. *J Am Chem Soc* 2013;135:1213-1216.
- [4] Liu H, Neal AT, Zhu Z, et al. Phosphorene: an unexplored 2D semiconductor with a high hole mobility. *ACS Nano* 2014;8:4033-4041.
- [5] Ahn CH, Rabe KM, Triscone JM. Ferroelectricity at the nanoscale: local polarization in oxide thin films and heterostructures. *Science* 2004;303:488-491.
- [6] Dawber M, Rabe KM, Scott JF. Physics of thin-film ferroelectric oxides. *Rev Mod Phys* 2005;77:1083-1130.
- [7] Fong DD, Stephenson GB, Streiffer SK, et al. Ferroelectricity in ultrathin perovskite films. *Science* 2004;304:1650-1653.
- [8] Lee D, Lu H, Gu Y, et al. Emergence of room-temperature ferroelectricity at reduced dimensions. *Science* 2015;349:1314-1317.
- [9] Junquera J, Ghosez P. Critical thickness for ferroelectricity in perovskite ultrathin films. *Nature* 2003;422:506-509.
- [10] Wu M, Zeng XC. Intrinsic ferroelasticity and/or multiferroicity in two-dimensional phosphorene and phosphorene analogues. *Nano Lett* 2016;16:3236-3241.
- [11] Chang K, Liu J, Lin H, et al. Discovery of robust in-plane ferroelectricity in atomic-thick SnTe. *Science* 2016;353:274-278.
- [12] Wang H, Qian X. Two-dimensional multiferroics in monolayer group IV monochalcogenides. *2D Mater* 2017;4:015042.

- [13] Shirodkar SN, Waghmare UV. Emergence of ferroelectricity at a metal-semiconductor transition in a 1T monolayer of MoS₂. *Phys Rev Lett* 2014;112:157601.
- [14] Luo W, Xu K, Xiang H. Two-dimensional hyperferroelectric metals: a different route to ferromagnetic-ferroelectric multiferroics. *Phys Rev B* 2017;96:235415.
- [15] Ding W, Zhu J, Wang Z, et al. Prediction of intrinsic two-dimensional ferroelectrics in In₂Se₃ and other III₂-VI₃ van der Waals materials. *Nat Commun* 2017;8:14956.
- [16] Wang X, Xiao C, Yang C, et al. Ferroelectric control of single-molecule magnetism in 2D limit. *Sci Bull* 2020;65:1252-1259.
- [17] Chandrasekaran A, Mishra A, Singh AK, Ferroelectricity, antiferroelectricity, and ultrathin 2D electron/hole gas in multifunctional monolayer MXene. *Nano Lett* 2017;17:3290-3296.
- [18] Xu B, Xiang H, Xia Y, et al. Monolayer AgBiP₂Se₆: an atomically thin ferroelectric semiconductor with out-plane polarization. *Nanoscale* 2017;9:8427-8434.
- [19] Qi J, Wang H, Chen X, et al. Two-dimensional multiferroic semiconductors with coexisting ferroelectricity and ferromagnetism. *Appl Phys Lett* 2018;113:043102.
- [20] Lai Y, Song Z, Wan Y, et al. Two-dimensional ferromagnetism and driven ferroelectricity in van der Waals CuCrP₂S₆. *Nanoscale* 2019;11:5163-5170.
- [21] Liu F, You L, Seyler KL, et al. Room-temperature ferroelectricity in CuInP₂S₆ ultrathin flakes. *Nat Commun* 2016;7:12357.
- [22] Sharma P, Xiang FX, Shao DF, et al. A room-temperature ferroelectric semimetal. *Sci Adv* 2019;5:eaax5080.
- [23] Fei Z, Zhao W, Palomaki TA, et al. Ferroelectric switching of a two-dimensional metal. *Nature* 2018;560:336-339.
- [24] Anderson PW, Blount EI. Symmetry considerations on martensitic transformations: 'ferroelectric' metals? *Phys Rev Lett* 1965;14:217-219.
- [25] Shi Y, Guo Y, Wang X, et al. A ferroelectric-like structural transition in a metal. *Nat Mater* 2013;12:1024-1027.
- [26] Sakai H, Ikeura K, Bahramy MS, et al. Critical enhancement of thermopower in a chemically tuned polar semimetal MoTe₂. *Sci Adv* 2016;2:e1601378.

- [27] Filippetti A, Fiorentini V, Ricci F, et al. Prediction of a native ferroelectric metal. *Nat Commun* 2016;7:11211.
- [28] Wang H, Qian X. Ferroicity-driven nonlinear photocurrent switching in time-reversal invariant ferroic materials. *Sci Adv* 2019;5:eaav9743.
- [29] Wang H, Qian X. Ferroelectric nonlinear anomalous hall effect in few-layer WTe_2 . *npj Comp Mater* 2019;5:119.
- [30] Xiao J, Wang Y, Wang H, et al. Berry curvature memory through electrically driven stacking transitions. *Nat Phys* 2020.
- [31] Blöchl PE. Projector augmented-wave method. *Phys Rev B* 1994;50:17953-17979.
- [32] Kresse G, Furthmüller J. Efficient iterative schemes for ab initio total-energy calculations using a plane-wave basis set. *Phys Rev B* 1996;54:11169-11186.
- [33] Perdew JP, Burke K, Ernzerhof M. Generalized gradient approximation made simple. *Phys Rev Lett* 1996;77:3865-3868.
- [34] Dong XJ, You JY, Gu B, et al. Strain-induced room-temperature ferromagnetic semiconductors with large anomalous hall conductivity in two-dimensional $\text{Cr}_2\text{Ge}_2\text{Se}_6$. *Phys Rev Appl* 2019;12:014020.
- [35] You JY, Zhang Z, Gu B, et al. Two-Dimensional room-temperature ferromagnetic semiconductors with quantum anomalous hall effect. *Phys Rev Appl* 2019;12:024063.
- [36] Suykens JA, Vandewalle J. Least squares support vector machine classifiers. *Neural Process Lett* 1999;9:293-300.
- [37] Liaw A, Wiener M. Classification and regression by randomforest. *R News* 2002;2:18-22.
- [38] Freund Y, Schapire RE. A decision-theoretic generalization of on-line learning and an application to boosting. *J Comput Syst Sci* 1997;55:119-139.
- [39] Safavian SR, Landgrebe D. A survey of decision tree classifier methodology. *IEEE Trans Syst Man Cybern* 1991;21:660-674.
- [40] Friedman JH. Greedy function approximation: a gradient boosting machine. *Ann Stat* 2001;29:1189-1232.

- [41] Ma XY, Lewis JP, Yan QB, et al. Accelerated discovery of two-dimensional optoelectronic octahedral oxyhalides via high-throughput *ab initio* calculations and machine learning. *J Phys Chem Lett* 2019;10:6734-6740.
- [42] Lu S, Zhou Q, Guo Y, et al. Coupling a crystal graph multilayer descriptor to active learning for rapid discovery of 2D ferromagnetic semiconductors/half-metals/metals. *Adv Mater* 2020;32:2002658.
- [43] Severson KA, Attia PM, Jin N, et al. Data-driven prediction of battery cycle life before capacity degradation. *Nat Energy* 2019;4:383-391.
- [44] Granda JM, Donina L, Dragone V, et al. Controlling an organic synthesis robot with machine learning to search for new reactivity. *Nature* 2018;559:377-381.
- [45] Gonze X, Lee C. Dynamical matrices, born effective charges, dielectric permittivity tensors, and interatomic force constants from density functional perturbation theory. *Phys Rev B* 1997;55:10355-10368.
- [46] Haastrup S, Strange M, Pandey M, et al. The computational 2D materials database: high-throughput modeling and discovery of atomically thin crystals. *2D Mater* 2018;5:042002.
- [47] Abrahams SC, Kurtz SK, Jamieson PB. Atomic displacement relationship to curie temperature and spontaneous polarization in displacive ferroelectrics. *Phys Rev B* 1968;172:551-553.
- [48] Li L, Salvador PA, Rohrer GS. Photocatalysts with internal electric fields. *Nanoscale* 2014;6:24-42.
- [49] Zhao P, Ma Y, Lv X, et al. Two-dimensional III₂-VI₃ materials: promising photocatalysts for overall water splitting under infrared light spectrum. *Nano Energy* 2018;51:533-538.
- [50] Mattheiss LF. Band structures of transition-metal-dichalcogenide layer compounds. *Phys Rev B* 1973;8:3719-3740.
- [51] Henkelman G, Uberuaga BP, Jónsson H. A climbing image nudged elastic band method for finding saddle points and minimum energy paths. *J Chem Phys* 2000;113:9901-9904.

- [52] Fei R, Kang W, Yang L. Ferroelectricity and phase transitions in monolayer group-IV monochalcogenides. *Phys Rev Lett* 2016;117:097601.
- [53] Guan S, Liu C, Lu Y, et al. Tunable ferroelectricity and anisotropic electric transport in monolayer β -GeSe. *Phys Rev B* 2018;97:144104.
- [54] Cui C, Hu WJ, Yan X, et al. Intercorrelated in-plane and out-of-plane ferroelectricity in ultrathin two-dimensional layered semiconductor In_2Se_3 . *Nano Lett* 2018;18:1253-1258.
- [55] Komsa HP, Kotakoski J, Kurasch S, et al. Two-dimensional transition metal dichalcogenides under electron irradiation: defect production and doping. *Phys Rev Lett* 2012;109:035503.
- [56] Zhuravlev MY, Sabirianov RF, Jaswal SS, et al. Giant electroresistance in ferroelectric tunnel junctions. *Phys Rev Lett* 2005;94:246802.
- [57] Wang F, Liu J, Huang W, et al. Subthermionic field-effect transistors with sub-5 nm gate lengths based on van der Waals ferroelectric heterostructures. *Sci Bull* 2020;65:1444-1450.

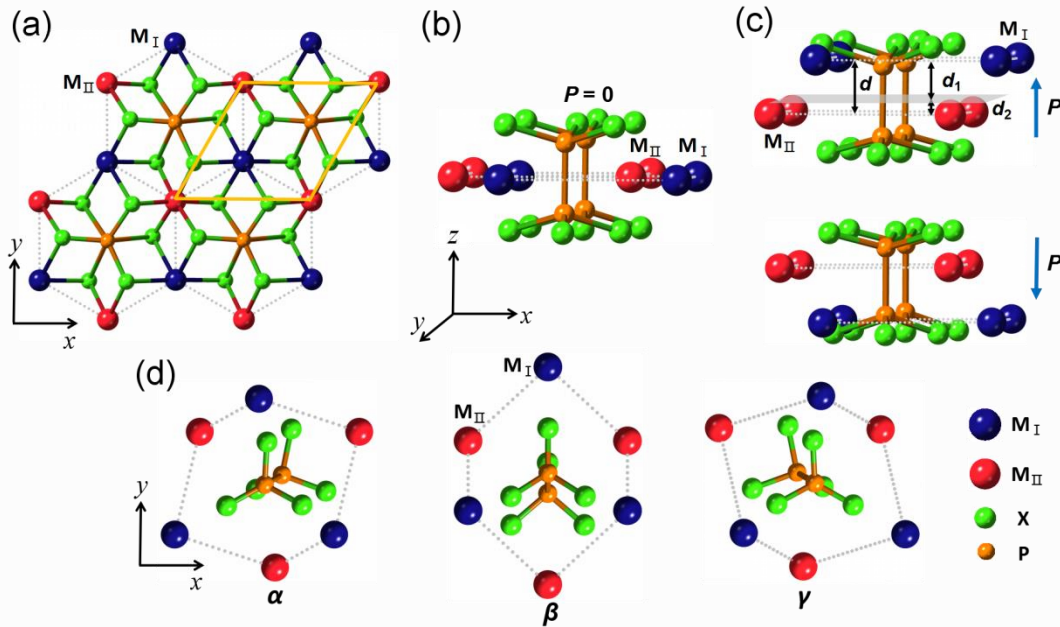


Fig. 1. Schematic structures of 2D bimetal phosphates ($M_I M_{II} P_2 X_6$, M_I and M_{II} atoms are different metal elements, $X=O, S, Se, Te$). The blue, red, green and orange balls represent M_I metal atoms, M_{II} metal atoms, chalcogen atoms, and phosphorus atoms, respectively. (a) Top view. The yellow parallelogram indicates the unit cell and dash lines denote a honeycomb lattice formed by metal atoms. P atoms sit at the center of the hexagons, and chalcogen atoms bridge metal atoms and P atoms. (b) Side view of the high-symmetry phase. (c) Side view of Type-I low-symmetry phases. d is the vertical displacement between M_I and M_{II} atoms. d_1 and d_2 , are the displacements of M_I and M_{II} atoms related to the bisect plane (indicated with grey color) of P-P pairs. The blue arrows (up/down) indicate the directions of out-of-plane electric polarization (P). (d) Top view of Type-II low-symmetry phases. The distorted structure with P-P pairs inclining along different directions forms three symmetry-equivalent phases (α , β and γ), respectively.

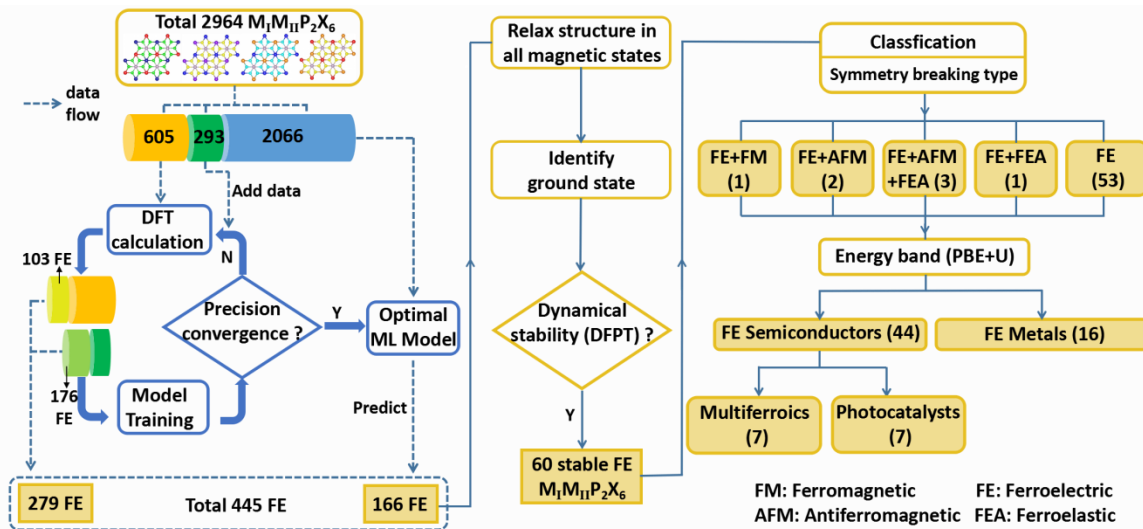


Fig. 2. The schematic procedure for discovering ferroelectric materials $M_I M_{II} P_2 X_6$. The left panel is the flowchart of the data-driven machine learning process, which generates an optimal machine learning model and obtains 445 potential ferroelectrics. In the right panel, 60 stable ferroelectric materials $M_I M_{II} P_2 X_6$ are obtained after dynamically stability screening, which are further classified into different types of ferroelectrics, and finally, 16 ferroelectric metals are figured out.

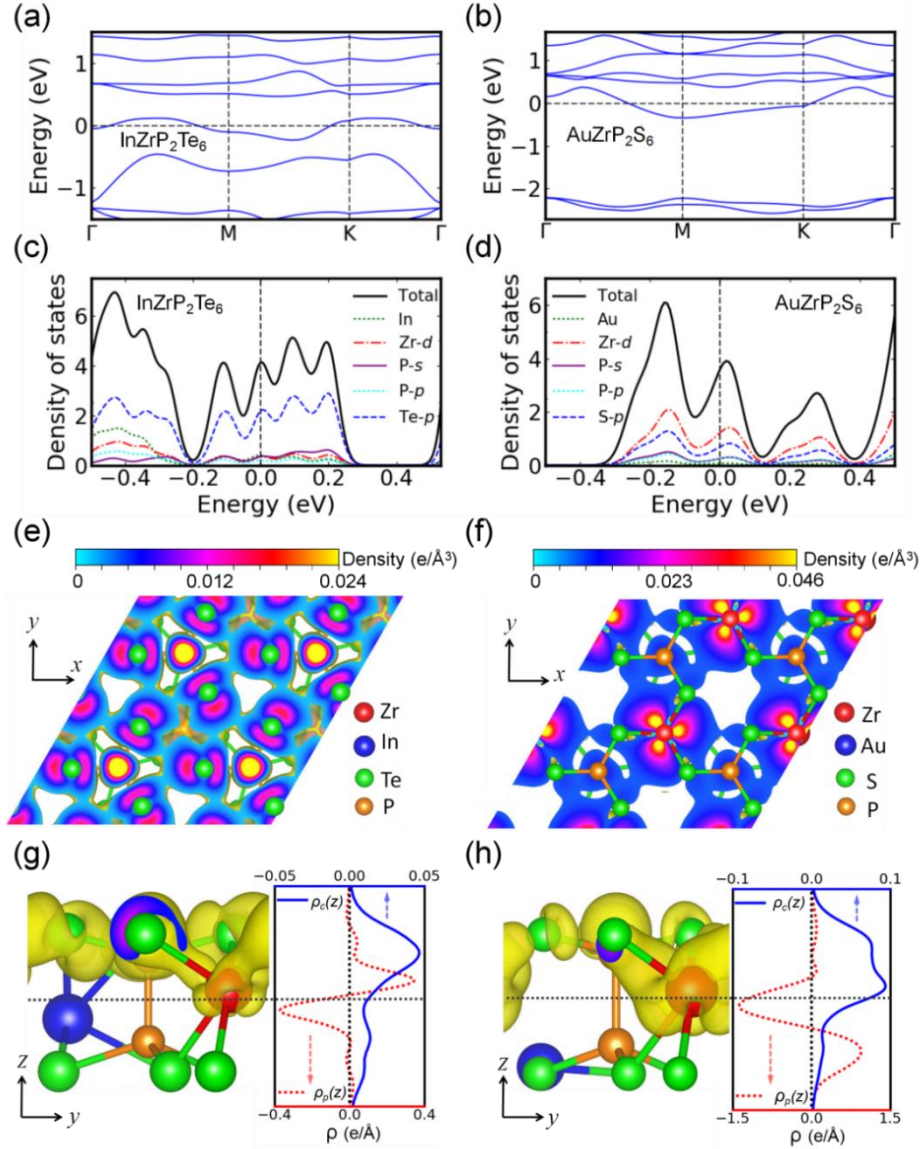


Fig. 3 Electronic properties of two ferroelectric metals: $\text{InZrP}_2\text{Te}_6$ and AuZrP_2S_6 . (a, b) Band structures at PBE+U level. (c, d) Projected density of states (PDOS). (e, f) and left panels of (g, h) are top and side views of partial electron density within energy range $|E - E_f| < 0.05$ eV, i.e., $\rho_c(\vec{r})$, respectively. In right panels of (g, h), blue lines indicate the reduced conducting electron density $\rho_c(z)$, and red dash lines indicate the reduced “FE-PE electron density difference” $\rho_p(z)$, where the vertical axis denotes the spatial z coordinate that is the same as in geometrical structures of corresponding left panels.

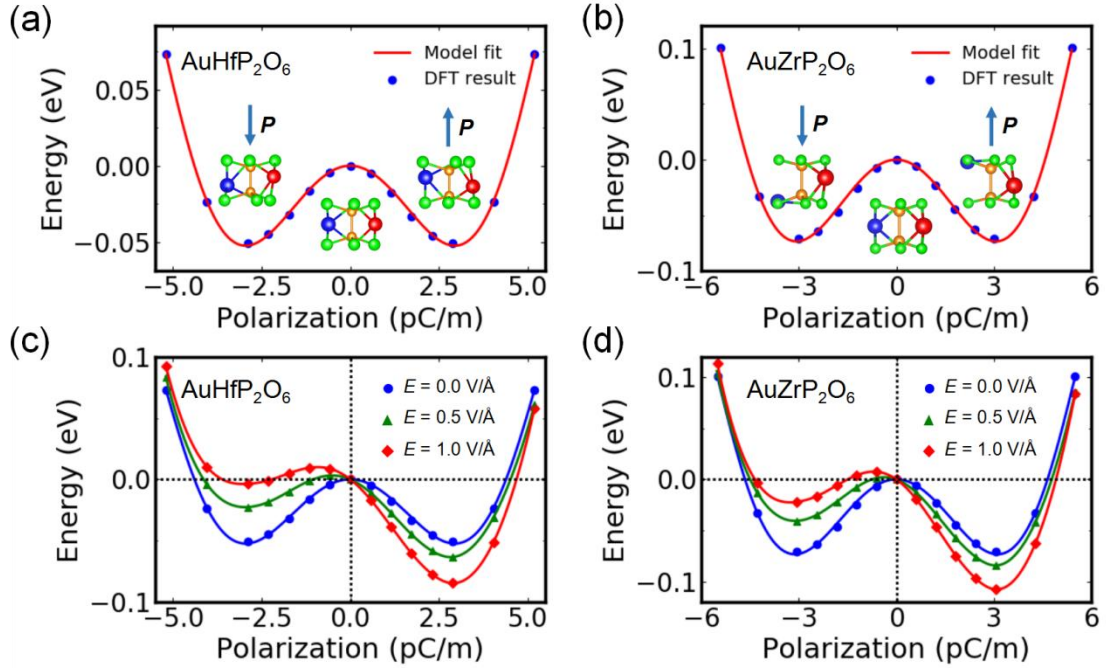


Fig. 4. Energy versus polarization of two ferroelectric metals (AuHfP_2O_6 and AuZrP_2O_6) and the effects of external electric field. (a, b) Energy versus polarization of two ferroelectric metals. The barrier between ferroelectric and paraelectric phases is presented. Blue points are the DFT-calculated total energies. The red lines are fitted curves with Landau-Ginzburg model. The directions of polarization (\mathbf{P}) in ferroelectric phases are marked by blue arrows. (c, d) Energy versus polarization of two ferroelectric metals under different vertical external electric fields. Points are the DFT-calculated total energies, and the lines are fitted curves.

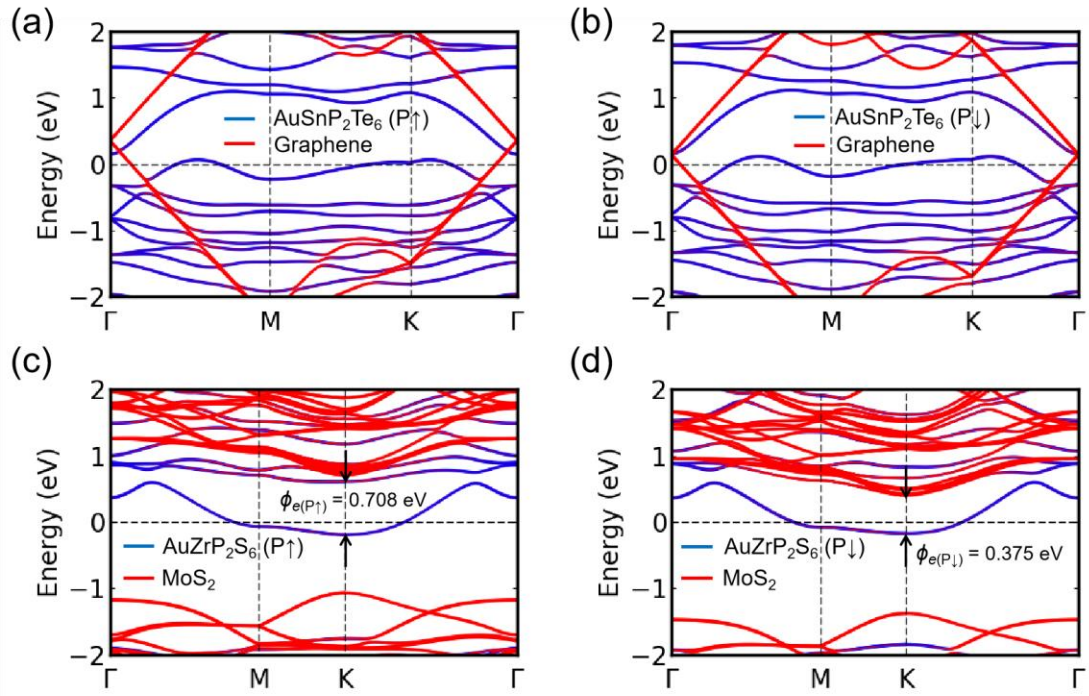


Fig. 5. Band structures of heterostructures. (a, b) AuSnP₂Te₆/Graphene. (c, d) AuZrP₂S₆/MoS₂. The directions of polarization (P) in ferroelectric metals are marked by black thin arrows. The blue and red colors indicate the contributions from different 2D materials.

Table 1 Properties of 16 ferroelectric metals.

Formula	Space group	d (Å)	d_1 (Å)	d_2 (Å)	Polarization (pC/m)/ (eÅ/unit cell)	Barrier (eV/unit cell)	N_e / unit cell
InPbP ₂ Te ₆	P3	1.16	0.61	0.55	0.570 (0.017)	0.360	53
SnYP ₂ Te ₆	P3	0.67	0.42	0.25	0.840 (0.025)	0.169	53
GaSnP ₂ Te ₆	P3	0.88	0.47	0.41	1.009 (0.028)	0.249	53
GaZrP ₂ Te ₆	P3	0.66	0.42	0.24	1.191 (0.034)	0.145	53
GaHfP ₂ Te ₆	P3	0.58	0.40	0.18	1.353 (0.038)	0.148	53
InSnP ₂ Te ₆	P3	1.08	0.61	0.47	1.610 (0.046)	0.420	53
InZrP ₂ Te ₆	P3	0.80	0.52	0.28	1.822 (0.053)	0.195	53
InHfP ₂ Te ₆	P3	0.71	0.49	0.22	1.916 (0.056)	0.187	53
PbYP ₂ Te ₆	P3	0.72	0.47	0.25	2.131 (0.064)	0.175	53
AuHfP ₂ O ₆	P3m1	0.67	0.62	0.05	2.888 (0.045)	0.044	61
AuZrP ₂ O ₆	P3m1	0.74	0.69	0.05	3.009 (0.047)	0.063	61
AgZrP ₂ S ₆	P3	0.94	0.78	0.16	3.010 (0.064)	0.096	61
CuHfP ₂ Se ₆	P3	1.47	1.36	0.11	5.463 (0.123)	0.146	61
CuZrP ₂ S ₆	P3	1.54	1.39	0.15	5.884 (0.121)	0.182	61
AuZrP ₂ S ₆	P3	1.83	1.63	0.20	9.740 (0.206)	0.573	61
AuSnP ₂ Te ₆	P3	2.09	1.77	0.32	9.828 (0.269)	0.365	61
Bilayer WTe ₂	Pm	-	-	-	0.423 (0.0058)	0.0006	-

Note: d is the vertical relative-displacement between M_I and M_{II} metal atoms along z -direction as indicated in Fig. 1c. d_1 and d_2 are the absolute values of displacements of M_I and M_{II} atoms when taking the bisecting plane of P - P pair as a reference, and $d_1 + d_2 = d$. The polarizations are listed in two different units. The ferroelectric-paraelectric transition barriers and number of total valence electrons (N_e) are also listed. The properties of bilayer WTe₂ are listed for comparison, which are obtained with the same method.